Bacterial responses and material-cell interplays with novel MoAlB@MBene

Michal Jakubczak, Dominika Bury, Verónica Montes-García, Artur Ciesielski, Michael Naguib, Agnieszka Jastrzębska

Bacterial responses and material-cell interplays with novel MoAlB@MBene

Michał Jakubczak, Dominika Bury, Verónica Montes-García, Artur Ciesielski, Michael Naguib, Agnieszka M. Jastrzębska**

M. Jakubczak, D. Bury, A. M. Jastrzębska
Warsaw University of Technology, Faculty of Mechatronics, św. Andrzeja Boboli 8, 02-525 Warsaw, Poland
E-mail: michal.jakubczak.dokt@pw.edu.pl, agnieszka.jastrzbska@pw.edu.pl

M. Jakubczak, D. Bury
Warsaw University of Technology, Faculty of Materials Science and Engineering, Wołoska 141, 02-507 Warsaw, Poland

Verónica Montes-García, Artur Ciesielski
Institut de Science et d'Ingénierie Supramoléculaires (I.S.I.S.), Université de Strasbourg & CNRS, 8 allée Gaspard Monge, 67000 Strasbourg, France

Artur Ciesielski
Centre for Advanced Technologies, Adam Mickiewicz University, Uniwersytetu Poznańskiego 10, 61-614 Poznań, Poland

M. Naguib
Department of Physics and Engineering Physics, Tulane University, New Orleans, LA 70118, USA

M. Naguib
Department of Chemistry, Tulane University, New Orleans, LA 70118, USA

Keywords: nanomaterials, MBene, bioactivity, bacteria, antibacterial properties

Developing efficient antibacterial nanomaterials has potential across diverse fields, but requires a deeper understanding of material-bacteria interactions. In this study, a novel two-dimensional (2D) core-shell MoAlB@MBene structure was synthesized using a mild wet-chemical etching approach. The growth of *E. coli*, *S. aureus*, and *B. subtilis* bacteria in the presence of MoAlB@MBene decreased in a concentration-dependent manner, with a prolonged lag phase in the initial 6 h of incubation. Even under dark conditions, MoAlB@MBene triggered the formation of intercellular reactive oxygen species (ROS) and singlet oxygen ($^1O_2$) in bacteria, while the bacteria protected themselves by forming biofilm and altering cell morphology. The MoAlB@MBene showed consistent light absorption across the visible range and a distinctive UV absorption edge. We identified two types of band gaps: direct (1.67 eV) and indirect (0.74 eV), which facilitate complex light interactions with MoAlB@MBene. Exposure to simulated white light led to decreased viability rates of *E. coli* (20.6%), *S. aureus* (22.9%), and *B. subtilis* (21.4%). Altogether, the presented study increases the understanding of bacteria responses in the presence of light-activated 2D nanomaterials.

1. Introduction

Pathogenic bacteria pose a significant and widespread health challenge globally. [1] Based on data from 2019, bacterial infections were responsible for 7.7 million deaths worldwide. This represented roughly one-eighth of all global fatalities, ranking bacterial infections as the second most significant cause of death on a worldwide scale, surpassed only by ischemic heart disease. [2] Health concerns related to bacterial infections are particularly evident in developing countries due to poor sanitation, limited access to clean water, inadequate healthcare infrastructure, and malnutrition. [3-5]

In order to mitigate the negative impact of pathogenic bacteria on various areas of life, intensive research is conducted in the fields of chemistry, biology, medicine, and nanotechnology. [6] In this area, nanomaterials hold promise in combating pathogenic bacteria for several reasons. [7] Their increased surface area provides better interaction with bacteria cells, while two-dimensional (2D) offers sharp edges, which can disrupt bacterial cell membranes. [8-11] 2D nanomaterials can also be engineered into stimuli-responsiveness in order to boost their antibacterial action. [10, 12]

In this regard, 2D nanostructures with unique bioactivity are being developed, including MXenes. [13-15] These are 2D transition metal carbides, nitrides, and carbonitrides derived from their parental MAX phases. [16] MXenes' properties, such as their tunable surface chemistry and hydrophilic nature, facilitate their use as biocidal agents. [17-19] This was confirmed in the work of Rasool *et al.*, who reported a decrease in the viability of *Escherichia coli* and *Staphylococcus aureus* when exposed to a $Ti_3C_2T_x$ MXene (T_x stands for mixed surface terminations) concentration of 200 μg mL^{-1} within 4 h. [20] They noted that the antibacterial activity was associated with a decrease in cell integrity, the release of cytoplasmic contents, and the induction of oxidative stress. Rosenkranz *et al.* explored the possibility of photothermal antibacterial therapy using $Ti_3C_2T_x$ MXene. [21] They noted that a combination of a 100 μg mL^{-1} concentration with a 5-minute laser treatment completely immobilized *E. coli* and *S. aureus*. In our recent work we showed, that the superior optical properties of $Ti_3C_2T_x$ MXene enable the development of light-induced self-sterilizing coatings with antimicrobial potential. [22] Nonetheless, Ozulumba *et al.* postulated that the apparent biocidal effect of $Ti_3C_2T_x$ may be misleading, attributing it to the presence of post-synthesis residual acidic impurities. [23] Moreover, numerous studies have confirmed the low stability of MXenes, resulting in the formation of oxides (*e.g.*, TiO_2) on the surface of nanoflakes, which are responsible for the antibacterial effect. [24-27]

Nano-laminated layered materials hold great promise as an alternative to state-of-the-art biocidal agents and therapies. [8, 17, 28] However, the drawbacks of MXenes, such as low chemical stability under air and a misleading biocidal effect, are prompting scientists to search for more prospective alternatives. [29-31] In this context, MBenes have been gathering significant attention recently. [29] These are 2D transition metal borides obtained from their parent MAB phases. [32-33] MBenes were first postulated by Ade and Hillebrecht in 2015, who highlighted their structural analogy to MXenes. [33] However, their variable crystal symmetries, differences in the modes of 2D layer sandwiching and, most importantly, the presence of boron instead of carbon suggest that they will interact distinctly compared to MXenes when introduced into biological systems. [29, 32, 34-35] Moreover, their long-term chemical stability under relevant working conditions is crucial when exploring interactions with bacteria, as it ensures that the material maintains its integrity without degrading or releasing harmful byproducts, which could alter bacterial behavior, interfere with experimental results, or compromise the intended biological interaction. [29, 36-37]

The stoichiometric description of MBenes is derived from their parent thermodynamically stable MAB phases. They exhibit diverse chemical formulas, represented as $M_{n+1}AB_{2n}$ (212,

314, 426), M_4AB_4 (414), and MAB (111). [32, 37] Here, 'M' stands for an early transition metal, 'A' is a metal from group A of elements, and 'B' represents boron. [32, 37] Additionally, 15 ternary laminated boride phases with in-plane chemical ordering, represented by the general formula $(M'_{2/3}M''_{1/3})_2AlB_2$, have been theoretically predicted. [38] Despite the fact that MBenes can be obtained under milder conditions than MXenes, efficient synthesis methods have only recently been established. [29] For example, Majed *et al.* reported the synthesis of Mo_2AlB_2 from MoAlB MAB phase using hydrofluoric acid (HF). [39] Further treatment with sodium hydroxide (NaOH) resulted in partial etching, oxidation, and material perforation. Our team proposed an optimized top-down wet-chemical etching and delamination approach using a mixture of hydrochloric acid (HCl) and hydrogen peroxide (H_2O_2), yielding outstanding results. [37, 40] However, interactions of MBenes with biological systems, including bacteria, have not been reported. Considering the presence of biologically active boron in the layered structure, successful synthesis of MBenes not only represent a natural progression but also offer tremendous intrigue in exploring their bioactivity. [29, 41]

Hence, our study aims to explore the bioactivity of a novel 2D core-shell MoAlB@MBene structure. At first, we obtained MoAlB@MBene from its parental MAB phase with water-based acid etching using a mixture of HCl and H_2O_2. Further, we characterized the obtained material in terms of morphology, structure, elemental, and phase composition, as well as stability, and optical properties. Subsequently, we investigated its concentration-dependent bioactivity towards Gram-negative *E. coli* and Gram-positive *S. aureus* and *B. subtilis* bacteria. Additional tests, such as reactive oxygen species (ROS) assays and biosorption studies, aid in elucidating material-cell boundary effects. To reveal the enhanced light-induced antibacterial potential of the MoAlB@MBene, we conducted additional tests following activation by an extra light source.

2. Results and discussion

2.1. MoAlB@MBene' preparation and characterization

Recent reports detail efficient synthesis protocols for novel 2D MBene, overcoming their development challenges. [37, 39-40] This led to the exploration of the MBenes' properties, yet their impact on living organisms, including bacteria, remains unexplored. We have already highlighted the enormous potential of MBenes for applications in biotechnology and nanomedicine in our review paper. [29] But before delving into microbiological studies, we

characterized the as-synthesized MoAlB@MBene and its parental MAB phase, ensuring the synthesis efficacy. Our analysis covered morphology, structure, elemental and phase composition, surface chemistry, and optical properties of both the initial MAB-phase and the resulting etching product **(Figure 1)**.

High-resolution scanning electron microscopy (HR-SEM) micrographs (Figure 1a) revealed MoAlB phase microstructure with a grain size under 10 µm, resembling typical ceramics. At higher magnifications, its distinctive nanolayered structure, common in MAX and MAB phases, becomes evident. [16, 42-44] After a 48 h of etching with HCl/H_2O_2 the MAB phase transforms into an expanded multilayered structure (Figure 1b), displaying nanometric spaces between layers and slit-shaped pores. Similar to MXenes synthesis from MAX phases, this transformation can be linked to removing the Al layers, creating gaps between the Mo-B layers. [16, 45-46] The edges of these layers appear spiky and sharp **(Figure S1)**, contributing to potential interactions with bacteria, known as the nanoblade effect. [8, 12, 47-48]

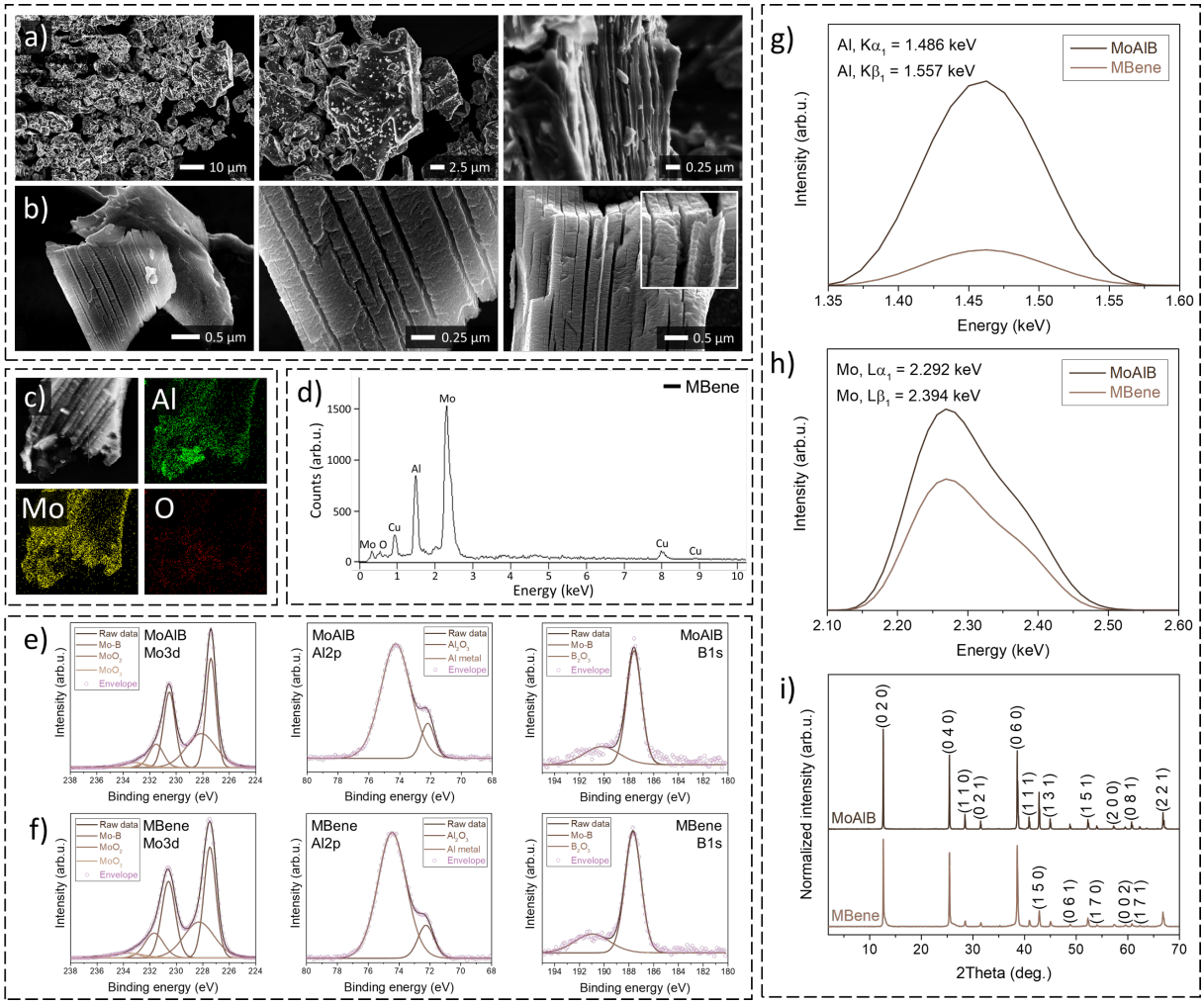

Figure 1. SEM micrographs representing **(a)** the parental MoAlB phase and **(b)** the resulting MoAlB@MBene. **(c)** The distribution of molybdenum (Mo), aluminum (Al), and oxygen (O)

obtained through EDS-mapping, accompanied by **(d)** the corresponding EDS spectrum. XPS peak fitting results for **(e)** MoAlB phase and **(f)** MoAlB@MBene showing Mo3d, Al2p, and B1s components. XRF studies showing alterations in **(e)** Al and **(f)** Mo in MoAlB@MBene, **(g)** X-ray diffractograms of MoAlB and MoAlB@MBene.

The energy-dispersive X-ray spectroscopy (EDS) mapping of etched MAB grain (Figure 1c) reveals the presence of MAB-associated elements **(Figure S2)** and uniform distribution of Mo and Al, except for localized regions with higher concentrations of Al. Minimal oxygen content indicates the MoAlB@MBene long-term stability, confirmed by EDS-spectrum (Figure 1d). Further, we noticed partial removal of Al from MoAlB, consistent with previous reports. [37, 40, 43] The amount of Al is half that of Mo, suggesting the removal of approximately one aluminum layer. However, the retained Al layers contribute to structural stability, enhancing performance and facilitating material studies. [37]

X-ray photoelectron spectroscopy (XPS) analysis is then conducted to quantify the amounts of Al, Mo, and B in the core-shell MoAlB@MBene (Figure 1e and f, also **Figure S3a**, as well as **Table S1** and **S2**). Unlike EDS, XPS has a typical penetration depth of 1 to 10 nm, enabling us to specifically quantify the composition of the surface or shell of the MoAlB@MBene. [49] The survey spectra revealed that in the MAB phase (Figure 1e and Table S1), the normalized atomic percentage ratio of Mo3d:B1s:Al2p was 1.05:1.00:2.63. After etching, this ratio shifted to 0.96:1.00:1.71 (Figure 1f and Table S2), indicating the loss of Al during the etching process. The high-resolution Mo3d, B1s and Al2p spectra of MoAlB MAB phase and core-shell MoAlB@MBene show considerable similarity. The Mo3d XPS spectra can be deconvoluted into three doublets, with the Mo—B component being the dominant one, accompanied by minor contributions from MoO_2 and MoO_3. Similarly, the B1s XPS spectra can be fitted with two components: the dominant Mo-B, along with a minor contribution from B_2O_3. The presence of molybdenum and boron oxides is consistent with previous experimental findings on MAB etching. Additionally, Al2p analysis revealed the presence of Al_2O_3 and Al metal on the MAB phase and core-shell MoAlB@MBene surface.

The X-ray fluorescence (XRF) technique (Figure 1g and h) confirmed the effective removal of Al during the 48 h etching of MoAlB, indicated by significant decrease in signal intensities. The selected etchant demonstrated selectivity, resulting in minimal Mo removal.

The X-ray diffraction (XRD) pattern of the MoAlB phase (Figure 1i) revealed an orthorhombic structure, with the presence of (020), (040), (110), (021), (060), (111), (150), (131), (061), (151), (170), (200), (002), (081), (171), and (221) planes, as indicated by peaks located at

diffraction angles of 12.68, 25.51, 28.52, 31.56, 38.65, 40.92, 42.89, 45.04, 48.87, 52.34, 54.06, 57.34, 59.55, 60.81, 62.38, and 66.89º, respectively. [33, 37, 39, 50-51] After etching, the intensity ratio of the characteristic peaks of the original MoAlB phase changed, indicating a partial removal of Al rather than a complete phase transformation. Importantly, the XRD pattern of MoAlB MBene is distinct from the typical XRD pattern of MoB MBene, suggesting that the Al layer is not fully removed, in full agreement with the EDS and XRF analysis.

The Fourier transform infrared (FT-IR) analysis (Figure S3b) of the MoAlB phase indicates that there are minimal functional groups present on the surface. Following synthesis, the etched product revealed vibrations indicating the presence of BO_3 and BO_4, as well as O-H functional groups. [37, 52-53] Details were included in the Supporting Information (SI) document.

The absorption spectrum (**Figure S4a**) acquired from the aqueous dispersion of MBene (Figure S4b) indicates comparable light absorption across the entire visible spectrum, with an absorption edge observed in the UV region. Subsequent studies on optical properties, conducted on solid samples and coupled with the Tauc method (check Figure S4c for absorption coefficient), revealed the presence of both direct and indirect band gaps. We calculated the direct band gap value to be 1.67 eV (Figure S4d), whereas for the indirect band gap, the value was determined to be 0.74 eV (Figure S4e). The obtained results suggest MBene's potential to be activated with additional light irradiation, which we took advantage of in our further studies. Dynamic light scattering (DLS) and particle shape analysis revealed the transformation of MAB due to the etching, which is evident in disruptions to the uniformity of MoAlB grains and suggests a heightened structural complexity and a deviation from the original MoAlB phase distribution. Details can be found in SI **(Figure S5 and Figure S6)**.

2.2. Exploring the bioactivity of MoAlB@MBene

After successfully synthesizing MoAlB@MBene, our studies explored the fascinating interplay between nanomaterials and bacteria, with potential implications in medicine, environmental science, and nanotechnology. While antibacterial properties are emphasized, some reports highlight beneficial bacteria-nanomaterials interactions within environmental settings. [8, 11, 18, 28, 54-57] For example, Tamez *et al.* found that applying inorganic nanoparticles at key stages of plant development can significantly boost growth, enhance crop yields, increase nutritional value, and help suppress diseases. [58] Likewise, Yin *et al.* showed that copper-contaminated sediments can be efficiently remediated with the use of titanium dioxide nanoparticles supported by granular activated carbon. [59]

Initial diffusion tests **(Figure S7 and Figure S8)** did not yield any clear information about the MoAlB@MBene bioactivity or material-cell interplays. Therefore, we examined how the various concentrations of MoAlB@MBene affect the development of bacteria by observing not only the changes in the initial cell count, but also alterations in growth dynamics. Thus, we determined growth curves in nutrient-rich (MHB broth) and nutrient-depleted (PBS) environments. The results are presented in **Figure 2**. Supporting Information document explains the experiment concept (*e.g.*, why error bars were omited, **Fig. S9**) and provides information about growth curves in a nutrient-depleted environment **(Figure S10)** and specific growth rate curves **(Figure S11)**.

Growth curves in nutrient-rich (Figure 2a, c, and e) and nutrient-depleted (Figure S10) environments show that MoAlB@MBene primarily influenced dynamics and kinetics while leaving the initial bacteria cells relatively unaffected. The OD at 610 nm, representing bacterial cell density, followed a sigmoidal pattern without MoAlB@MBene, which is to be expected. As MoAlB@MBene concentration increased, the sigmoidal curve sustained, tending to flatten at higher concentrations.

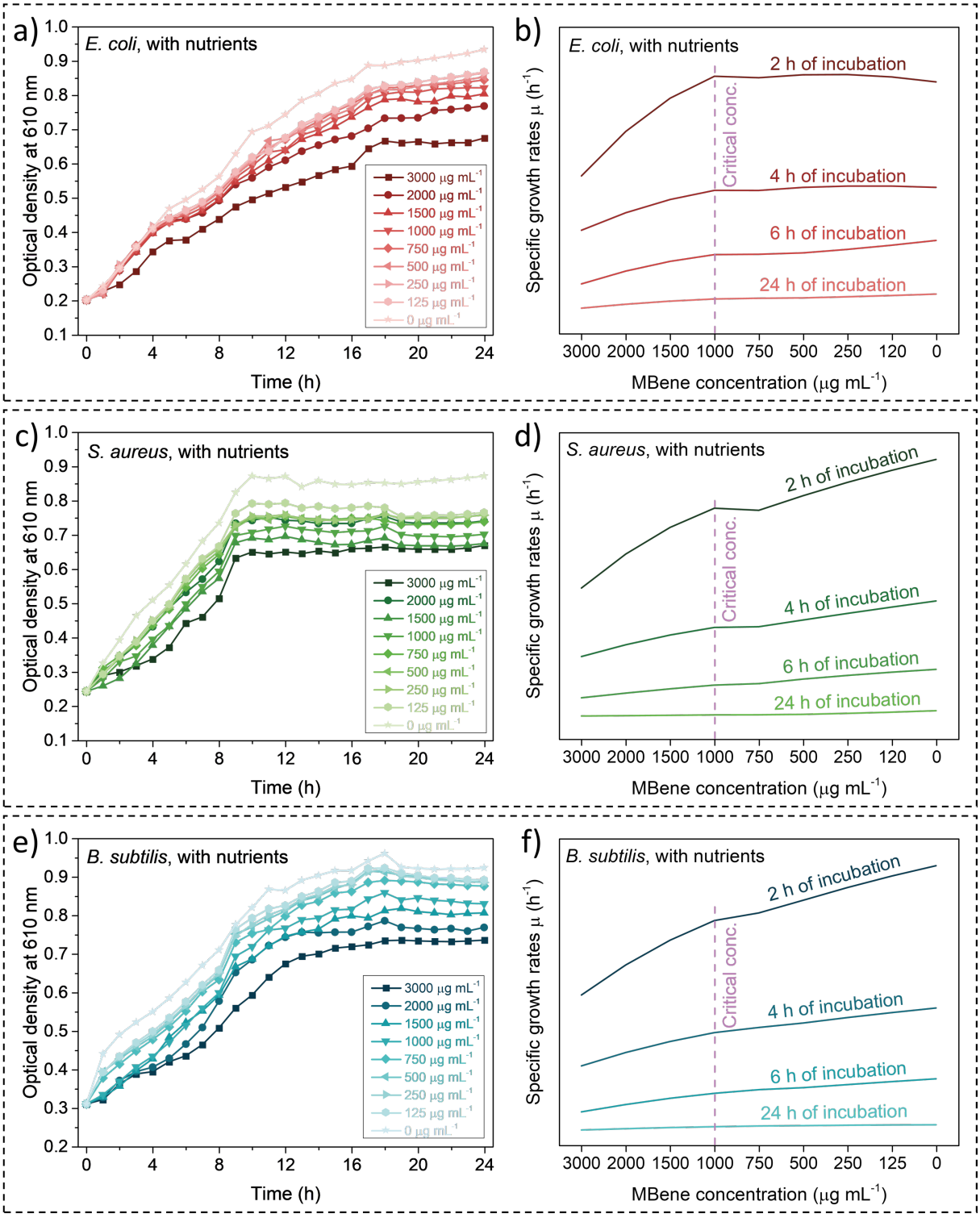

Figure 2. (a, c, e) The changes in the density of **(a)** *E. coli*, **(c)** *S. aureus*, and **(e)** *B. subtilis* suspensions when exposed to varying concentrations of MoAlB@MBene over time in a nutrient-rich environment, accompanied by **(b, d, f)** specific growth rate curves depending on the MoAlB@MBene concentration at selected time points. Purple line marks MoAlB@MBene concentration significantly altering bacteria growth kinetics. The measurement error did not exceed 10% on average.

MoAlB@MBene's impact on bacterial growth directly correlated with concentration, particularly 3000 µg mL^{-1}, diminishing as concentration decreased. The presence of MoAlB@MBene extended the lag phase, a period allowing bacteria to adapt to new environmental conditions. As described by Monod, the lag phase remains poorly understood and is controlled by unknown regulatory mechanisms. [60] Chatterjee *et al.* define this prolonged lag phase as delay time, indicating the duration for bacteria to reach the reproductive stage. [61] Figure 2 shows a significant increase in delay time with increasing MoAlB@MBene concentration for all three tested bacteria, with *B. subtilis* exhibiting the most noticeable increase.

Delay time was most pronounced in the initial 6 h of incubation. To understand how MoAlB@MBene concentration affects delay time, specific growth rate curves relative to the concentration were depicted (Figure 2b, d and f). Given the most disrupted growth dynamics in the first 6 h, we plotted specific growth rate curves every two h up to 6 h, and comparatively after 24 h of incubation. Time-based specific growth rate curves were shown in the SI (Figure S11).

From the 2 h incubation, the specific growth rate decreases dynamically at the higher MoAlB@MBene concentrations (3000 to 1000 µg mL^{-1}). Further concentration reduction caused a plateau (as seen in *E. coli* or *S. aureus*) or a less dynamic reduction (*B. subtilis*). Subsequent concentration reduction leads to a linear return to the parameter's value (*S. aureus* or *B. subtilis*) or nearly reaching the reference sample's value (*E. coli*). This suggests 1000 µg mL^{-1} concentration as critical (Figure 2b, d and f, purple line), below which there's a low impact on bacteria growth dynamics, affecting the delay time.

Over time, the impact of increasing MoAlB@MBene concentrations on the specific growth rates of tested bacteria diminished, as indicated by the curves plotted at 4 and 6 h of incubation. After 24 h, nearly identical values were observed, regardless of the MoAlB@MBene concentration. However, this doesn't signify that MoAlB@MBene ceased affecting the bacteria. Cultures incubated in the presence of bacteria (Figure 2a, c, and e) never reached the OD levels of control despite growth curves plateauing. These permanent changes resulted in a reduction in the maximum number of cells achievable in that system. Nonetheless, all bacteria could adapt to the presence of MoAlB@MBene, continuing to grow at a diminished rate. Similar adaptive responses have been observed for *E. coli* exposed to silver, TiO_2, and MoO_3 nanoparticles, as well as palladium oxide-modified nitrogen-doped TiO_2. [61-65] These studies highlight bacterial adaptability to various nanomaterials, underscoring the importance of nuanced analyses of long-term effects and underlying mechanisms in nanotoxicology studies.

Assessing viability over short incubation periods (2 to 6 h, **Figure S12**), the lowest viability occurred after 2 h, progressively rising. Variations were noted based on the nutrient presence, confirming MoAlB@MBene' predominant impact on growth dynamics. After 2 h incubation with 3000 µg mL^{-1} of MoAlB@MBene in a nutrient-rich environment, viability for *E. coli*, *S. aureus*, and *B. subtilis* was 76, 46, and 45%, respectively. In nutrient-depleted environments, viability didn't significantly deviate from 100%. Over 24 h **(Figure S13)**, consistent viability of approximately 60-70% for *E. coli*, 70-80% for S. *aureus*, and 80% for *B. subtilis* was noted, regardless of nutrient availability.

2.3. Intracellular ROS levels and singlet oxygen assay

Reported data suggests that 2D nanomaterials induce reactive oxygen species (ROS) within bacteria, leading to cell membrane damage and modifications in DNA, lipids, and proteins, causing cellular dysfunction and growth disturbances. [11, 17-18, 20, 28-29, 54, 66] Thus, to understand the inherent properties of the MoAlB@MBene, we performed our experiments fully in the darkness. Furthermore, concentration-dependent intracellular ROS and singlet oxygen ($^1O_2$) were tested in both nutrient-rich and nutrient-depleted environments to assess the nutrients impact. Tests were conducted after 2 and 6 h of incubation were conducted to observe short-term changes. Concentration-dependent intracellular ROS levels were presented in **Figure 3**, while **Figure S14** in SI shows concentration-dependent singlet oxygen production.

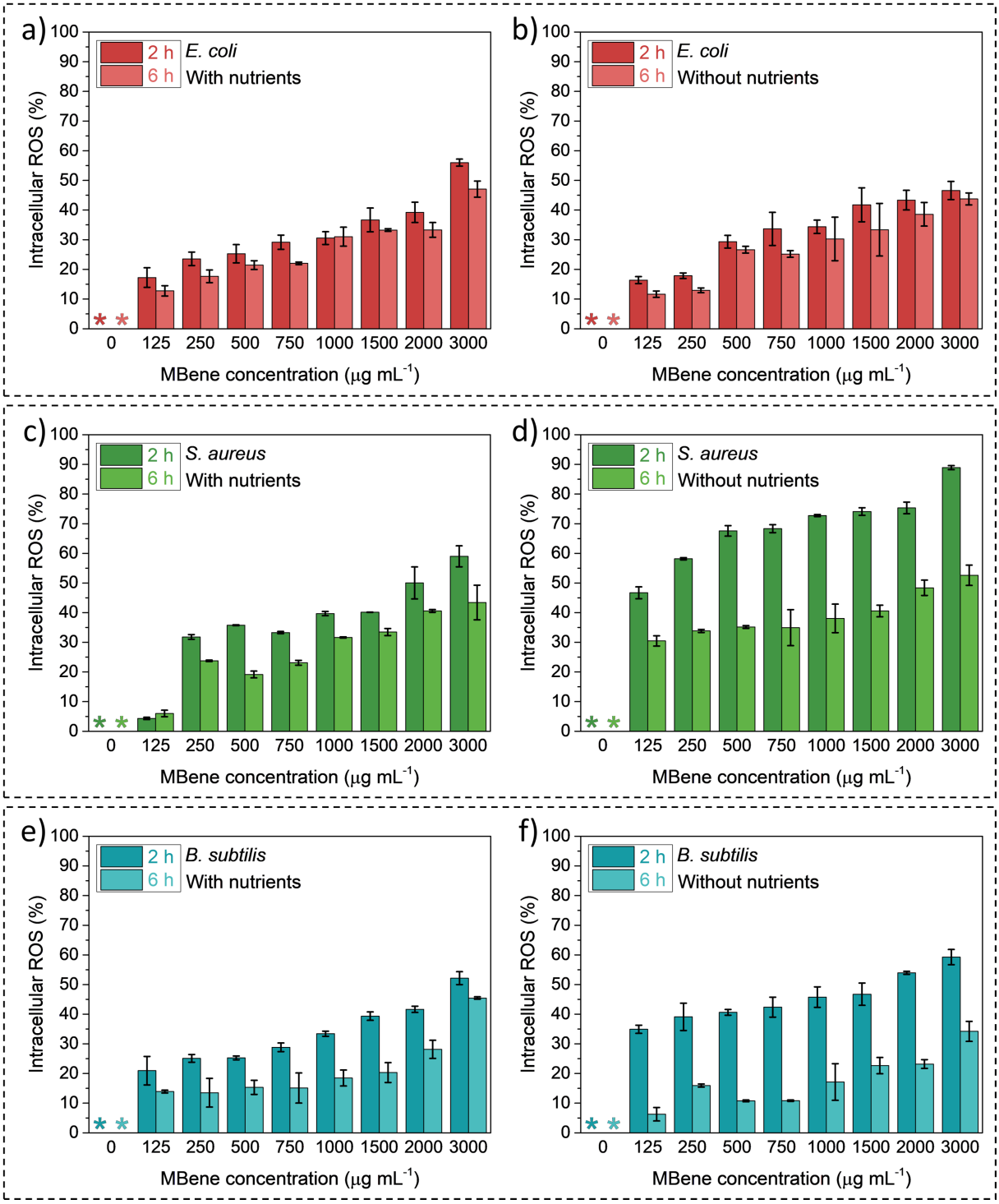

Figure 3. Concentration-dependent intracellular ROS levels after 2 and 6 h of incubation for **(a-b)** *E. coli*, **(c-d)** *S. aureus*, and **(e-f)** *B. subtilis* in **(a, c, e)** a nutrient-rich and **(b, d, f)** nutrient-depleted environments. Controls were marked with an asterisk (*), indicating a zero ROS assumption.

According to Figure 3, intercellular ROS level directly correlated with MoAlB@MBene concentration, peaking at 3000 μg mL^{-1}. Time-dependent intracellular ROS levels decreased with longer incubation (2 *vs* 6 h), more notably in nutrient-depleted environments, suggesting adaptive capabilities observed earlier. At the highest MoAlB@MBene concentration in nutrient-rich environments and after 2 h of incubation, intracellular ROS levels were 60% for *E. coli* and *B. subtilis* and at 50% for *S. aureus* (Figure 3a, c and e). After 6 h, ROS levels decreased to approximately 40-45% (Figure 3a, c and e). In nutrient-depleted environments (Figure 3b, d, and f), intracellular ROS levels were similar or higher, reaching nearly 90% for *S. aureus* after 2 h of incubation at 3000 μg mL^{-1}. Over time, ROS levels decreased to values similar to nutrient-rich environments.

The $^1O_2$ tests indicated an increasing trend with MoAlB@MBene concentration, notably accumulating over time. Only *B. subtilis* in a nutrient-depleted environment showed a decrease in the amount of $^1O_2$ during incubation, suggesting adaptive abilities. Despite MoAlB@MBene inducing ROS generation, bacteria counteracted oxidative stress induction over time, partially explaining the delay time observed in growth tests. Oxidative stress is a feature of the lag phase, with studies reporting the induction of superoxide dismutase during *E. coli* growth on agar and a similar oxidative stress response during *Salmonella enterica* lag phase in a liquid medium. [67-68]

Nanomaterials can trigger ROS generation and oxidative stress through various mechanisms. They interact with cells, causing DNA damage, altered cell signaling, and cytotoxicity, which disrupt cellular redox balance and increase ROS production. [69] Overproduction of ROS occurs not only in mitochondria but also through enzymatic reactions involving NADPH oxidases, xanthine oxidase, and peroxisomes. [70] Nanomaterials can damage antioxidant enzymes, leading to increased ROS accumulation and creating a vicious cycle of oxidative stress. [71-72] High-reactivity nanomaterials, such as nanotubes, can induce inflammation by acting as foreign bodies, leading to ROS release and further oxidative stress. [73]

2.4. Studies on biosorption properties

Our ROS studies provided initial insights into MoAlB@MBene-bacteria interactions, but we sought to investigate prolonged effects. For this, we examined the biosorption properties of MoAlB@MBene over 24, 48, and 72 h at a critical concentration (1000 μg mL^{-1}). This intermediate toxic level aimed to observe growth disturbances while minimizing the material's

direct influence. The resulting SEM micrographs were shown in **Figure 4** and in **Figure S15** in SI.

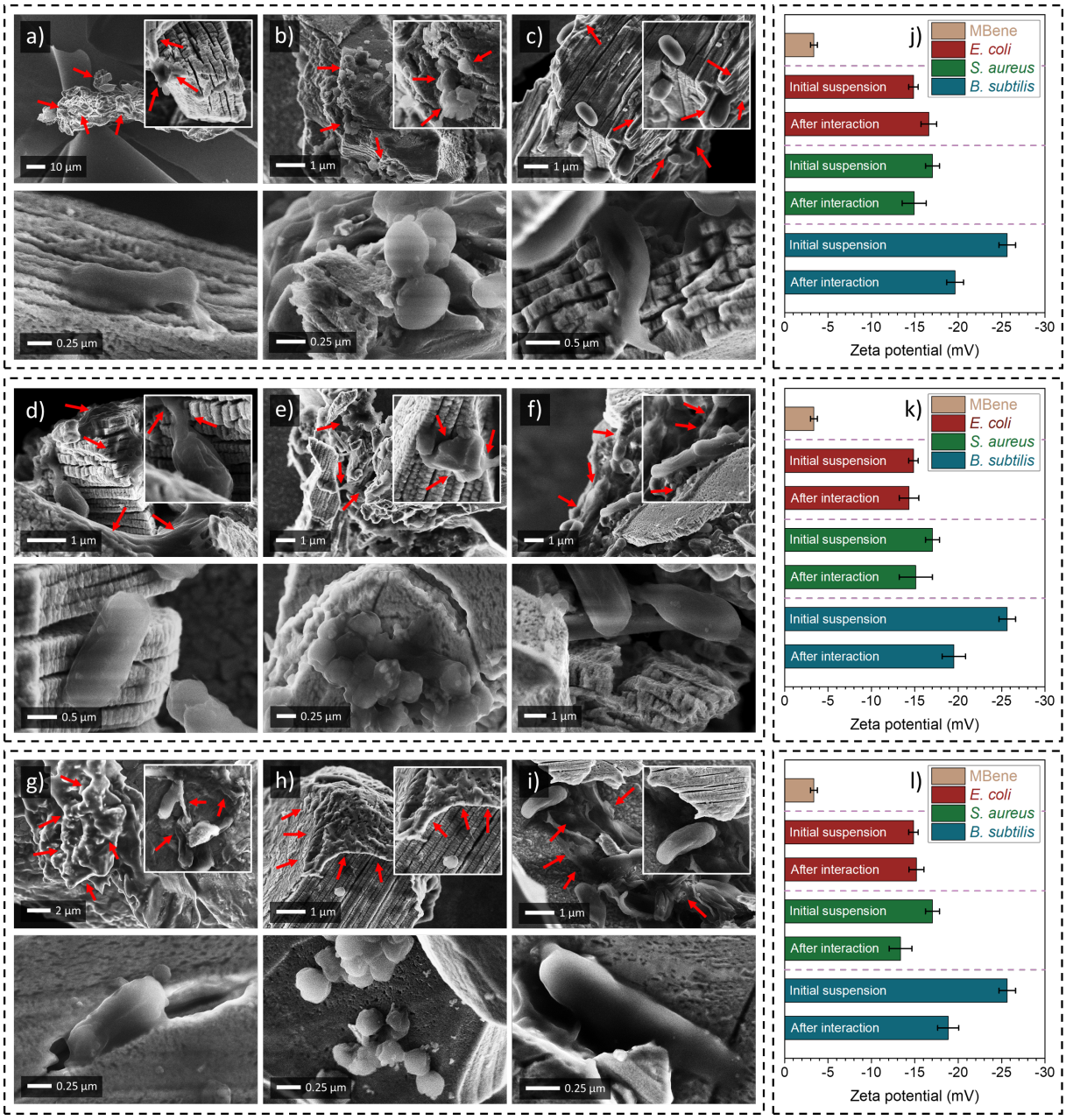

Figure 4. SEM micrographs of MoAlB@MBene after incubation with **(a, d, g)** *E. coli*, **(b, e, h)** *S. aureus* and **(c, f, i)** *B. subtilis* for **(a-c)** 24, **(d-f)** 48 and **(g-i)** 72 h. The red arrows indicate biofilm formation. Zeta potential measured after **(j)** 24, **(k)** 48 and **(l)** 72 h of incubation.

SEM micrographs (Figure 4a, b, and c) depict MoAlB@MBene samples incubated with *E. coli*, *S. aureus*, and *B. subtilis*. When incubated with MoAlB@MBene, *E. coli* (Figure 4a and Figure S15a) and *B. subtilis* (Figure 4c and Figure S15c) maintained their rod-like morphology, while

S. aureus (Figure 4b and Figure S15b) retained its typical cocci-like shape. Notably, all tested bacteria tend to grow in clusters, showing potential for biofilm formation. This is evident in *E. coli* (Figure 4a and Figure S15a) and *S. aureus* (Figure 4b and Figure S15b), where individual cells are challenging to separate, indicating a dominance of biofilm formation. *B. subtilis* (Figure 4c and Figure S15c) exhibited less intense biofilm formation, but we noticed cell collapse, indicating an unfavorable environment.

With extended incubation period (48 and 72 h), biofilm formation intensified, notably covering larger areas of MoAlB@MBene grains, especially for *E. coli* and *S. aureus* (Figure 4d, e, g, and h and Figure S15d, e, g, and h). Evidently, *B. subtilis* exhibited greater resistance, showing a lesser degree of biofilm formation. After 48 h (Figure 4f and Figure S15f), biofilm primarily forms along material edges, with clearly visible separate bacteria cells. By 72 h (Figure 4i and Figure S15i), biofilm formation extended inside the MoAlB@MBene cavities, with fewer distinctly visible separate cells.

During the incubation with MoAlB@MBene *E. coli* cells retained their rod-like shape but became noticeably narrower, appearing sunken, with wrinkled cell walls (Figure 4d, g and Figure S15d, g). For *S. aureus*, MoAlB@MBene had a pronounced and devastating effect, changing its cocci-like morphology to an irregular spherical shape after 48 and 72 h (Figure 4e, h and Figure S15e, h). *B. subtilis* maintained its rod-like morphology more effectively, with cells appearing firm initially and developing more surface wrinkles over prolonged incubation (Figure 4f, i and Figure S15f, i). Notably, all bacterial cells, regardless of the incubation duration, appeared covered with particles below 0.1 μm, possibly smaller MoAlB@MBene particles adsorbed onto the bacteria's surface.

The biosorption assay's second part involved zeta potential investigations to assess biofilm formation efficiency and bacterial coverage on the MoAlB@MBene surface. Zeta potential measures the electrical potential at the particle-liquid interface. If biofilm or bacterial adsorption occurs, the material's zeta potential should approach the one of bacteria. Compared zeta potential values for samples incubated in the presence of bacteria for 24, 48, and 72 h with pure bacterial suspension, and the material itself was presented in Figure 4j, k, and l, respectively.

Results indicate extensive bacterial settlement on the MoAlB@MBene surface, as seen in zeta potential values. Pure MoAlB@MBene had a zeta potential of approximately -3.5 mV, significantly differing from all bacteria-incubated samples. Across incubation time, MoAlB@MBene with *E. coli* showed nearly identical zeta potential to initial bacterial suspension. Similar observations were made with *S. aureus* for 24 and 48 h, but a noticeable

decrease after 72 h (difference of -3.5 mV) suggests bacterial metabolic dysfunction, consistent with SEM micrographs. The largest zeta potential differences, averaging -7 mV, were observed with *B. subtilis*, aligning with SEM observations of low biofilm formation and the presence of individual cells.

Biofilms, communities of microorganisms encased in self-produced matrices, serve as a survival strategy for bacteria in unfriendly environments. Facilitating adherence, colonization, and resource sharing, biofilm formation provides advantages of protection and defense, increasing persistence and longevity. [74] Mann *et al.* demonstrated *Pseudomonas aeruginosa* adaptative abilities on prolonged exposures to silver nanoparticles and ionic silver (Ag^+), developing persistent cells through biofilm formation. [75] Zhang *et al.* observed *E. coli* adapting to TiO_2 nanoparticles through biofilm formation and cell remodeling, enhancing stress tolerance. [63] These findings align with our studies, highlighting the crucial role of biofilm formation and cell remodeling in challenging environments.

2.5. Light-induced tunable bioactivity

Further, we explored the light-activated bioactivity of MoAlB@MBene. Our recent study highlighted its exceptional photocatalytic performance in decomposing methylene blue. [40] Consequently, we aimed to extend this potential to biology-related research, investigating MoAlB@MBene's applicability for *in-situ* immobilization of bacteria upon light activation. Using white light (WH) to simulate environmental conditions, we employed 1000 μg mL^{-1} of MoAlB@MBene. Samples without MoAlB@MBene served as the negative control, with a dark environment for comparison. **Figure 5** shows changes in bacterial density, specific growth rates, and viability due to MoAlB@MBene light activation in a nutrient-rich environment. Results for nutrient-depleted environment were shown in SI **(Figure S16** and **Figure S17)**.

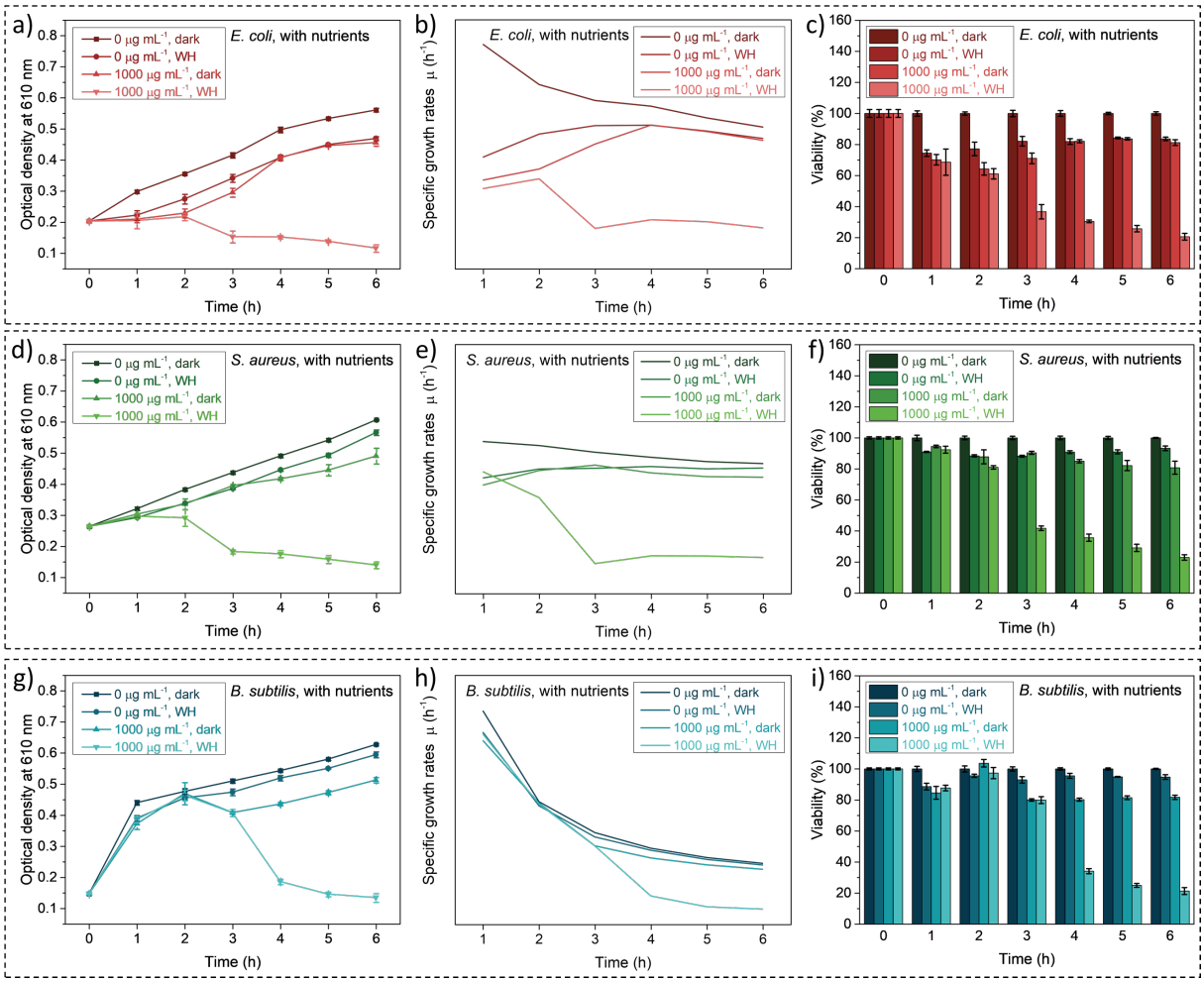

Figure 5. (a, d, g) The changes in the density of **(a)** *E. coli*, **(d)** *S. aureus*, and **(g)** *B. subtilis* suspensions exposed to MoAlB@MBene and white light (WH) over time in a nutrient-rich environment. For comparison we presented results for MBene and control sample in the dark, and exposed to white light. **(b, e, h)** Corresponding specific growth rate curves over time. **(c, f, i)** The viability changes for **(c)** *E. coli*, **(f)** *S. aureus*, and **(i)** *B. subtilis* bacteria exposed to MoAlB@MBene and white light, compared to reference, and incubated in darkness, in nutrient-rich environment.

Analyzing optical density (OD) changes for *E. coli* (Figure 5a), *S. aureus* (Figure 5d), and *B. subtilis* (Figure 5g), the influence of light and MoAlB@MBene becomes evident. Compared to the dark control, the lag phase extension was observed, but both light-exposed control and MoAlB@MBene in darkness eventually resumed stable growth. Specific growth rate curves (Figure 5b, e, and h) showed light-alone lag phase extension: 1 h for *E. coli* and *S. aureus*, and 2 h for *B. subtilis*. Comparatively, for MoAlB@MBene in darkness these effects persisted: 4 h (*E. coli*), 1 h (*S. aureus*), and 2 h (*B. subtilis*).

The synergy of white light and MoAlB@MBene emerged as a game-changer, efficiently immobilizing bacteria *in-situ*. When exposed to either light or MoAlB@MBene in darkness, bacterial viability consistently ranged between 80-90% (Figure 5c, f, and i). These results are consistent with the growth curves observed during experiments conducted in the dark (Figure 2a, c, and e). However, combining MoAlB@MBene with light significantly affected viability. Following 6 hours of irradiation, viability reductions were observed: *E. coli* to 20.6%, *S. aureus* to 22.9%, and *B. subtilis* to 21.4% (Figure 5c, f and i, respectively). In the nutrient-depleted environment, a consistent trend of decreasing density was observed with MoAlB@MBene and light irradiation (Figure S16), while controls and samples exposed to irradiation alone or MBene in darkness maintained consistent culture density values (within the margin of error), as shown in section 2.2 (Figure S11). Viability reduction after 6 hours in the nutrient-depleted environment was: 78.4% for *E. coli*, 67.5% for *S. aureus*, and 80.0% for *B. subtilis* (Figure S17a, b, and c, respectively), aligning with nutrient-rich environment results.

The use of photocatalysis for bacteria elimination is an active research field. When a semiconductor photocatalyst absorbs light with energy equal to or greater than its band gap, electron-hole pairs are generated. These pairs separate into positively charged holes (h^+) in the valence band (VB) and electrons (e^-) in the conduction band (CB). The VB XPS spectra (**Figure S18a** and **b** in SI) show that the VB of MoAlB@MBene is 1.65 eV. Using the formula $E_{CB} = E_{VB} - Eg$, the CB of MoAlB@MBene is calculated to be -0.02 eV. As illustrated in the band structure diagram (Figure S18c in SI), holes can generate ROS by converting adsorbed water to •OH, while CB electrons can reduce molecular oxygen to produce $^1O_2$ or reduce H_2O_2 to form •OH. These generated ROS can interact with bacterial membrane lipids, proteins, and DNA. [22, 76] The bacteria's antioxidants are insufficient to neutralize the ROS, leading to oxidative stress, DNA degradation, lipid peroxidation, protein oxidation, and ultimately cell death. [77-78]

3. Conclusion

To summarize, we successfully synthesized MoAlB@MBene by employing the top-down chemical etching procedure on the parent MoAlB phase, using HCl and H_2O_2 mixture. SEM studies confirmed the multilayered structure of the MoAlB@MBene, exihbting distinct spiky-like, sharp edges. SEM-EDS, XPS and XRF analyses demonstrated the preferential removal of Al over Mo from the MoAlB phase, while XRD investigations revealed a reduction in characteristic MoAlB phase peaks. FT-IR assessments indicated the pristine surface chemistry

of MBene, free from molecules introduced after synthesis or significant oxidation. UV-Vis spectroscopy showcased consistent material absorption across the visible range, featuring a distinct absorption peak in the UV region, as well as the presence of both direct and indirect band gaps at 1.67 and 0.74 eV, respectively.

The presence of MoAlB@MBene led to concentration-related disrupted growth and an elongated lag phase observed within the first 6 h of the bioactive studies. After 2 h of incubation, it became evident that the highest concentration of MBene (3000 μg mL^{-1}) resulted in a reduction of *E. coli* viability by 24%, *S. aureus* by 54%, and *B. subtilis* by 55%.

Concentration-based studies highlighted a correlation between ROS levels and the concentration of MoAlB@MBene. For instance, exposure to 3000 μg mL^{-1} of MoAlB@MBene resulted in *E. coli* and *B. subtilis* exhibiting intracellular ROS levels of 60%, while *S. aureus* displayed 50% in a nutrient-rich environment. Over time, a tendency toward ROS reduction was observed, partially explaining the elongated lag phase.

SEM investigations into MoAlB@MBene's biosorption properties revealed rapid adsorption of all bacteria, leading to the formation of a protective biofilm primarily near the material edges. Over time, biofilm formation increased with bacteria aggregating into larger cell clusters, deviating from their usual morphology. Zeta potential studies confirmed efficient saturation of the material with bacteria cells. Nevertheless, *B. subtilis* displayed higher resistance to the impact of MoAlB@MBene compared to *E. coli* and *S. aureus*.

In the final stage of our study, we validated the bioactivity of the MoAlB@MBene through light activation. We demonstrated that the prolonged lag time can be heightened upon exposure to light. This leads to continual *in-situ* inhibition of existing bacterial activity and prevents the real-time formation of new cells. During the 6 h of the experiment, we observed that the viability of *E. coli* decreased to 20.6%, *S. aureus* to 22.9%, and *B. subtilis* to 21.4%. This represents nearly a fourfold increase compared to the same concentration of MBene without light stimulation.

Light-induced antibacterial materials, such as developed MoAlB@MBene have numerous potential applications due to their ability to control microbial growth on demand. [22] These materials can be used as coatings on hospital surfaces, medical devices, and surgical instruments to significantly reduce hospital-acquired infections by continuously eliminating bacteria. [79-80] They are also effective in water purification systems, providing both filtration and disinfection through light-induced reactions that generate reactive oxygen species. [18] Additionally, these materials can be integrated into consumer products like textiles, personal

care items, and food packaging to maintain hygiene, reduce bacterial growth, and extend product shelf life. [81-82]

4. Experimental Section/Methods

MoAlB MAB phase synthesis: The MoAlB MAB phase utilized in this study was derived from precursor powders, which included molybdenum boride (MoB) and aluminum with a size of less than 44 μm. All powders were obtained from Alfa Aesar (Ward Hill, MA, USA). Firstly, MoB and aluminum powders were mixed in a Turbula T2F mixer at a ratio of 1:1.2 for a 3 h at a 56 rpm, and in the presence of 10 mm yttria-stabilized zirconia balls. Further, the resulting powder was shaped into 12 grams pellets. These pellets were then placed in a tube furnace and subjected to a gradual heating process (10 °C min^{-1} heating rate), reaching temperatures of 750 °C and subsequently 1500 °C, each for a duration of 2 h, all while maintaining a continuous argon flow at a rate of 100 sccm. Following the thermal treatment, the solid samples obtained were allowed to cool down to room temperature and grounded to a particle size of less than 44 μm.

Development of the core-shell MoAlB@MBene: The mixture of 9 M hydrochloric acid (HCl) and 0.3% hydrogen peroxide (H_2O_2) was prepared in a beaker and cooled in an ice bath to prevent overheating. Next, MoAlB powder was gently introduced into the beaker with continuous stirring (1 g of MAB per 100 mL of solution). Within the initial 10 minutes, a substantial amount of O_2 bubbles appeared. The reaction was allowed to continue for 48 h, as this time, we found it to yield the most efficient synthesis. [40] During this process, the originally dark MoAlB powder changed its color to slightly more grey. Subsequently, the solution was washed with double-distilled (DDI) water until the pH reached 7, achieved through centrifugation at 5000 rpm. The resulting sediment was then redispersed in isopropyl alcohol to prevent further oxidation and stored in a dark environment at -44 °C for future use. The powdered form of MoAlB@MBene was prepared using the freeze-drying method.

Characterization of the as-synthesized MAB phase and MoAlB@MBene: The morphology and structure were examined with HR-SEM using a Hitachi S-5500 (Hitachi, Tokyo, Japan) and an accelerating voltage of 5.0 kV. We also used the above mentioned equipment to assess the elemental composition with SEM-EDS (Scanning Electron Microscopy with Energy-Dispersive X-ray Spectroscopy), as well as performing elemental mapping.

The chemical composition of the samples was studied using X-ray photoelectron spectroscopy (XPS). XPS analyses were performed using a Thermo Scientific KAlpha X-ray photoelectron spectrometer (Waltham, MA, USA) with an aluminium X-ray source (energy 1.4866 keV) and working at 10^{-8} - 10^{-9} mbar pressure in the main chamber. The X-ray spot size was settled at 400 μm. The samples were prepared by drop-casting onto conductive copper tape and dried under nitrogen (N_2). All XPS spectra were calibrated using the C1s peak at 284.8 eV as a reference.

X-ray diffraction patterns (XRD) were obtained from drop-casted samples using a BrukerD8 X-ray diffractometer (Bruker, Billerica, MA, USA), Cu K_α=1.54060 Å. The analysis covered an angular range from 2 to 70 degrees, with increments of 0.03 degrees.

The studies of the partial elements etching from the MAB phase were carried out using the XRF spectrometer (PI 100, Polon-Izot, Warsaw, Poland). The spectrometer was fitted with a 125–140 eV resolution silicon drift detector (SSD), a test tube containing a rhodium (Rh) anode, and a multilayer 50 keV monochromator. The analysis was carried out in ambient air conditions, with a 300 sec measurement time allocated for each sample, along with a 100 sec normalization period.

Exploring the bioactivity of MoAlB@MBene: A time- and concentration-dependent assay of biocidal action was conducted using the principle of serial dilution and by subsequently measuring optical density at 610 nm (OD_{610}). Studies were performed with PBS and MHB to evaluate the impact of nutrient presence on MoAlB@MBene bioactivity. For this purpose, a stock solution of MoAlB@MBene was prepared in either PBS or MHB. Subsequently, we created serial dilutions from stock solution in multiwell plates, and bacterial solution in PBS or MHB (details from bacteria preparation can be found in SI) was added to achieve a final concentration equivalent to McFarland Standard No. 1 in each well. The following concentrations of MoAlB@MBene were prepared: 3000, 2000, 1500, 1000, 750, 500, 250, and 125 μg mL^{-1}. Pure PBS or MHB was employed as the negative control. Bacterial growth was studied by plotting OD values over time, allowing for the examination of bacterial growth kinetics. The experiments were conducted in eight repetitions, and averages were reported.

The prepared cultures were incubated at 37 ± 2 °C for 72 h, and under constant shaking of 150 rpm, and changes in OD_{610} were measured using an Infinite 200 PRO multiplate reader (Tecan, Männedorf, Switzerland). The OD alterations were monitored each h for up to 24 h to illustrate the dynamics of bacterial growth changes, whereas control measurements were also conducted at 24, 48, and 72 h. The alterations of bacterial growth dynamics were studied based on results

from the time- and concentration-dependent assay. Such alternations were determined by the specific growth rates μ calculated from **Equation 1**:

$$\mu\ (h^{-1}) = \frac{ln(OD_n) - ln(OD_c)}{t_x - t_0} \quad (1)$$

Where: t_0 is the time of test start, t_x is the time in which measurement was performed, OD_n is the optical density of the studied sample at time t_x, OD_c is the average optical density of the control sample at time t_0. The obtained OD values were also utilized to calculate the relative cell viability V **(Equation 2)**:

$$V\ (\%) = \frac{a_n}{a_c} \times 100 \quad (2)$$

Where: a_n is the OD value of the sample with studied concentration of MoAlB@MBene at a given point in time, a_c is the OD value of the control sample at a given point in time.
For further studies, we selected a concentration of 1000 μg mL^{-1} of MoAlB@MBene, as it demonstrated the most potential in the conducted studies.

Intracellular ROS levels and singlet oxygen assay: The intracellular ROS levels and $^1O_2$ assay were performed with fluorescent indicators. From the acquired kinetics, we selected the 2 and 6 h time points as the most representative for understanding the observed results. The intracellular ROS levels were assessed using the CM-H_2DCFDA fluorescent probe (Thermo Fisher Scientific, Waltham, MA, USA), which was dissolved in dimethyl sulfoxide (DMSO, 99.99% pure, Chempur, Piekary Śląskie, Poland). Subsequently, 100 μL of the bacterial suspension exposed to MoAlB@MBene or control was transferred to the multiwell plate, and the CM-H_2DCFDA was added to achieve the concentration of 2 μM in each well. We also monitored the hypothetical potential for the formation of $^1O_2$ using the Singlet Oxygen Sensor Green fluorescent reagent (Thermo Fisher Scientific, Waltham, MA, USA). Details were included in SI. In the last step, the samples were incubated in the dark for 30 min. To assess intracellular ROS levels and $^1O_2$ levels, we measured fluorescence intensity using a multiplate reader. For both cases, excitation and emission wavelengths of 485 nm and 520 nm, respectively, were utilized. Levels of intracellular reactive oxtgen species (ROS) and $^1O_2$ were calculated using **Equation 3**:

$$N\ (\%) = \frac{A}{B} \times 100 \quad (3)$$

Where: A represents the fluorescent intensity of the investigated sample, and B represents the fluorescent intensity of the reference sample.

Studies on biosorption properties: For the sample preparation, we utilized the protocol developed in our laboratory, which has been previously reported. [83-84] Briefly, bacterial pellets were washed multiple times and resuspended in dechlorinated and filtered (0.22 μm) tap water, with further adjustment to McFarland Standard No. 2. Next, dispersions of MoAlB@MBene were prepared in the same tap water within Eppendorf tubes (Eppendorf, Hamburg, Germany) and sterilized using a UV-C biocidal lamp. After that 100 μL of the prepared bacterial suspensions were added, which, due to the halfway dilution with the MoAlB@MBene suspension, resulted in a final McFarland Standard No. 1. After mixing, the samples were incubated for 24, 48, and 72 h at 37 ± 2 °C (separate samples were prepared).
After the specified incubation time, an additional 100 μL of water was added, and 75 μL of 2.5% glutaraldehyde (Sigma-Aldrich, Saint Louis, MO, USA) was employed. Subsequently, such prepared samples were left overnight at 4 °C. In the last step, multiple washes were performed on the samples to eliminate any cells that were not firmly attached. Such prepared samples were further analyzed using qualitative SEM observations and quantitative zeta potential studies. Before SEM studies, samples were gradually dehydrated with increasing ethanol concentrations (12.5, 25, 50, 75, and 100%). Further samples were studied with HR-SEM Hitachi S-5500 (Hitachi, Tokyo, Japan) using an accelerating voltage of 5.0 kV. To maintain cellular metabolic functions, glutaraldehyde fixation was excluded in the sample preparation for quantitative studies, avoiding overnight treatment. The Zetasizer Nano ZS analyzer (Malvern Instruments, Malvern, UK) was utilized, employing the Smoluchowski model. Measurements were taken at 25 °C, with each measurement repeated 10 times for accuracy. The final results were presented as the mean value of the zeta potential ± SD.

Light-induced tunable bioactivity: The experiment was conducted in 4 mL glass vials (UV-C sterilized). The 2 mL of a sterile stock solution of MoAlB@MBene in either PBS or MHB, and 2 mL of a stock bacterial solution (McFarland standard No. 2) were introduced into the vials; thus, the bacterial suspension reached McFarland standard No. 1 in each vial. Then, the vials were placed in a photochemical reactor (PhotoCube™, ThalesNano, Budapest, Hungary) and

exposed to simulated daylight (wavelength range: 400−700 nm, luminous flux: 5920 lm, and input power: 128 W per LED) for 6 h at 37 ± 2 °C with continuous stirring (150 rpm). Changes in OD were monitored every h by measuring absorbance at 610 nm with microplate reader Infinite 200 PRO (Tecan, Männedorf, Switzerland). A sample without MoAlB@MBene served as the negative control. The experiment was performed as triplicates and average values were reported. Bacterial growth was studied by plotting OD values over time. Specific growth rates and relative cell viability were calculated using **Equation 1** and **Equation 2**, respectively.

Supporting Information

Supporting Information is available from the Wiley Online Library or from the author.

Data availability statement

The data that support the findings of this study are openly available in Repository for Open Data RepOD at https://doi.org/10.18150/BWFTNA, reference number doi:10.18150/BWFTNA.

Acknowledgements

This work was funded by National Science Centre (NCN) within the framework of the research project ‘OPUS-18’ (UMO-2019/35/B/ST5/02538).

MJ and AMJ acknowledge the financial support from the research project ‘OPUS-18’ (UMO-2019/35/B/ST5/02538). M.J. acknowledges funding from the National Science Centre, within the framework of the research project ‘PRELUDIUM-22’ (UMO-2023/49/N/ST11/03574). MJ and DB acknowledge the financial support from the Foundation for Polish Science (FNP, Scholarship START program) and the ID-UB project (Scholarship Plus program). D.B. further acknowledges funding from the National Science Centre, within the framework of the research project ‘PRELUDIUM-21’ (UMO-2022/45/N/ST5/02906).

MJ is also grateful to his student, Iga Niewiadomska, for her assistance during the XRF measurements.

Conflict of interest statement

The authors declare no conflicts of interest.

Received: ((will be filled in by the editorial staff))
Revised: ((will be filled in by the editorial staff))
Published online: ((will be filled in by the editorial staff))

References

[1] R. E. Baker, A. S. Mahmud, I. F. Miller, M. Rajeev, F. Rasambainarivo, B. L. Rice, S. Takahashi, A. J. Tatem, C. E. Wagner, L.-F. Wang, A. Wesolowski, C. J. E. Metcalf, *Nat. Rev. Microbiol.* **2022**, 20, 193.
[2] *Lancet* **2022**, 400, 2221.
[3] B. Aslam, W. Wang, M. I. Arshad, M. Khurshid, S. Muzammil, M. H. Rasool, M. A. Nisar, R. F. Alvi, M. A. Aslam, M. U. Qamar, M. K. F. Salamat, Z. Baloch, *Infect. Drug. Resist.* **2018**, 11, 1645.
[4] T. E. Nagel, B. K. Chan, D. De Vos, A. El-Shibiny, E. K. Kang'ethe, A. Makumi, J.-P. Pirnay, *Front. Microbiol.* **2016**, 7.
[5] C. K. Pooi, H. Y. Ng, *npj Clean Water* **2018**, 1, 11.
[6] M. Alavi, D. Kahrizi, F. Martinez, M. Rai, *Front. Microbiol.* **2023**, 14.
[7] T. Hu, X. Mei, Y. Wang, X. Weng, R. Liang, M. Wei, *Science Bulletin* **2019**, 64, 1707.
[8] M. Jakubczak, A. M. Jastrzębska, *Front Chem* **2021**, 9, 685014.
[9] M. Jakubczak, E. Karwowska, A. Fiedorczuk, A. M. Jastrzębska, *RSC Advances* **2021**, 11, 18509.
[10] M. Jakubczak, D. Bury, A. Wojciechowska, E. Karwowska, A. M. Jastrzębska, *Mater. Chem. Phys.* **2023**, 297, 127333.
[11] P. Kumar, P. Huo, R. Zhang, B. Liu, *Nanomaterials (Basel)* **2019**, 9.
[12] M. A. K. Purbayanto, M. Jakubczak, D. Bury, V. G. Nair, M. Birowska, D. Moszczyńska, A. Jastrzębska, *ACS Applied Nano Materials* **2022**, 5, 5373.
[13] K. Salimiyan rizi, *J. Mol. Struct.* **2022**, 1262, 132958.
[14] M. Jakubczak, D. Bury, M. A. K. Purbayanto, A. Wójcik, D. Moszczyńska, K. Prenger, M. Naguib, A. M. Jastrzębska, *Scientific Reports* **2022**, 12, 14366.
[15] D. Bury, M. Jakubczak, R. Kumar, D. Ścieżyńska, J. Bogacki, P. Marcinowski, A. M. Jastrzębska, *MRS Bull.* **2023**, 48, 271.
[16] M. Naguib, M. Kurtoglu, V. Presser, J. Lu, J. Niu, M. Heon, L. Hultman, Y. Gogotsi, M. W. Barsoum, *Advanced Materials* **2011**, 23, 4248.
[17] A. Szuplewska, D. Kulpińska, M. Jakubczak, A. Dybko, M. Chudy, A. Olszyna, Z. Brzózka, A. M. Jastrzębska, *Advanced Drug Delivery Reviews* **2022**, 182, 114099.
[18] K. Rasool, R. P. Pandey, P. A. Rasheed, S. Buczek, Y. Gogotsi, K. A. Mahmoud, *Materials Today* **2019**, 30, 80.
[19] T. Wojciechowski, A. M. Jastrzębska, A. S. Vasilchenko, M. Jakubczak, M. Wolska-Pietkiewicz, A. Rozmysłowska-Wojciechowska, D. Moszczyńska, A. Olszyna, W. Ziemkowska, *Nano-Structures & Nano-Objects* **2022**, 29, 100820.
[20] K. Rasool, M. Helal, A. Ali, C. E. Ren, Y. Gogotsi, K. A. Mahmoud, *ACS Nano* **2016**, 10, 3674.
[21] A. Rosenkranz, G. Perini, J. Y. Aguilar-Hurtado, D. F. Zambrano, B. Wang, B. Niccolini, P. C. Henriques, E. Rosa, F. De Maio, G. Delogu, M. De Spirito, V. Palmieri, M. Papi, *Applied Surface Science* **2021**, 567, 150795.
[22] M. Jakubczak, D. Bury, A. Wojciechowska, J. Mitrzak, K. Budnik, D. Moszczyńska, A. M. Jastrzębska, *Journal of Alloys and Compounds* **2024**, 976, 173318.
[23] T. Ozulumba, G. Ingavle, Y. Gogotsi, S. Sandeman, *Biomater. Sci.* **2021**, 9, 1805.

[24] K. Rasool, K. A. Mahmoud, D. J. Johnson, M. Helal, G. R. Berdiyorov, Y. Gogotsi, *Scientific Reports* **2017**, 7, 1598.
[25] M. Jakubczak, E. Karwowska, A. Rozmysłowska-Wojciechowska, M. Petrus, J. Woźniak, J. Mitrzak, A. M. Jastrzębska, *Materials* **2021**, 14, 182.
[26] A. Iqbal, J. Hong, T. Y. Ko, C. M. Koo, *Nano Convergence* **2021**, 8, 9.
[27] D. Bury, M. Jakubczak, M. A. K. Purbayanto, A. Wojciechowska, D. Moszczyńska, A. M. Jastrzębska, *Small Methods* **2023**, 7, 2201252.
[28] S. Szunerits, R. Boukherroub, *Journal of Materials Chemistry B* **2016**, 4, 6892.
[29] M. Jakubczak, A. Szuplewska, A. Rozmysłowska-Wojciechowska, A. Rosenkranz, A. M. Jastrzębska, *Advanced Functional Materials* **2021**, 31, 2103048.
[30] M. Malaki, X. Jiang, H. Wang, R. Podila, H. Zhang, P. Samorì, R. S. Varma, *Chemical Engineering Journal* **2023**, 463, 142351.
[31] F. Seidi, A. Arabi Shamsabadi, M. Dadashi Firouzjaei, M. Elliott, M. R. Saeb, Y. Huang, C. Li, H. Xiao, B. Anasori, *Small* **2023**, 19, 2206716.
[32] V. G. Nair, M. Birowska, D. Bury, M. Jakubczak, A. Rosenkranz, A. M. Jastrzębska, *Advanced Materials* **2022**, 34, 2108840.
[33] M. Ade, H. Hillebrecht, *Inorganic Chemistry* **2015**, 54, 6122.
[34] A. Carlsson, J. Rosen, M. Dahlqvist, *Physical Chemistry Chemical Physics* **2022**, 24, 11249.
[35] B. Zhang, J. Zhou, Z. Sun, *Journal of Materials Chemistry A* **2022**, 10, 15865.
[36] R. Álvarez-Chimal, V. I. García-Pérez, M. A. Álvarez-Pérez, R. Tavera-Hernández, L. Reyes-Carmona, M. Martínez-Hernández, J. Á. Arenas-Alatorre, *Arabian Journal of Chemistry* **2022**, 15, 103804.
[37] M. Jakubczak, A. Wojciechowska, D. F. Zambrano, D. Moncada, M. Birowska, D. Moszczyńska, K. Eisawi, M. Naguib, A. Rosenkranz, A. M. Jastrzębska, *Applied Materials Today* **2023**, 35, 101925.
[38] J. Zhou, J. Palisaitis, J. Halim, M. Dahlqvist, Q. Tao, I. Persson, L. Hultman, P. O. Å. Persson, J. Rosen, *Science* **2021**, 373, 801.
[39] A. Majed, M. Torkamanzadeh, C. F. Nwaokorie, K. Eisawi, C. Dun, A. Buck, J. J. Urban, M. M. Montemore, V. Presser, M. Naguib, *Small Methods* **2023**, 7, 2300193.
[40] D. Bury, M. Jakubczak, M. A. K. Purbayanto, M. Rybak, M. Birowska, A. Wójcik, D. Moszczyńska, K. Eisawi, K. Prenger, V. Presser, M. Naguib, A. M. Jastrzębska, *Adv. Funct. Mater.* **2023**, DOI: 10.1002/adfm.202308156.
[41] M. Białek, M. Czauderna, K. A. Krajewska, W. Przybylski, *Journal of Animal and Feed Sciences* **2019**, 28, 307.
[42] S. Gupta, M. Fuka, Cham **2018**.
[43] L. T. Alameda, P. Moradifar, Z. P. Metzger, N. Alem, R. E. Schaak, *Journal of the American Chemical Society* **2018**, 140, 8833.
[44] L. T. Alameda, C. F. Holder, J. L. Fenton, R. E. Schaak, *Chemistry of Materials* **2017**, 29, 8953.
[45] M. Naguib, J. Come, B. Dyatkin, V. Presser, P.-L. Taberna, P. Simon, M. W. Barsoum, Y. Gogotsi, *Electrochemistry Communications* **2012**, 16, 61.
[46] M. Naguib, V. N. Mochalin, M. W. Barsoum, Y. Gogotsi, *Advanced Materials* **2014**, 26, 992.
[47] T. Malina, E. Maršálková, K. Holá, J. Tuček, M. Scheibe, R. Zbořil, B. Maršálek, *Carbon* **2019**, 155, 386.
[48] H. I. Hamouda, M. S. Selim, S. A. Higazy, S. Shabana, Z. Hao, C. Liu, *Synth. Met.* **2023**, 296, 117349.
[49] D. N. G. Krishna, J. Philip, *Applied Surface Science Advances* **2022**, 12, 100332.

[50] O. Shi, L. Xu, A. Jiang, Q. Xu, Y. Xiao, D. Zhu, S. Grasso, C. Hu, *Ceramics International* **2019**, 45, 2446.
[51] K. J. Baumler, O. S. Adams, R. E. Schaak, *Chemical Communications* **2023**, 59, 4814.
[52] C. C. Zhang, X. Gao, B. Yilmaz, *Catalysts* **2020**, 10, 1327.
[53] A. L. James, K. Jasuja, *RSC Advances* **2017**, 7, 1905.
[54] E. Karwowska, *Nanotechnology Reviews* **2017**, 6, 243.
[55] V. L. Colvin, *Nature Biotechnology* **2003**, 21, 1166.
[56] M. R. Wiesner, G. V. Lowry, K. L. Jones, M. F. Hochella, Jr., R. T. Di Giulio, E. Casman, E. S. Bernhardt, *Environ Sci Technol* **2009**, 43, 6458.
[57] F. Ameen, K. Alsamhary, J. A. Alabdullatif, S. Alnadhari, *Ecotoxicol. Environ. Saf.* **2021**, 213, 112027.
[58] C. Tamez, N. Zuverza-Mena, W. Elmer, J. C. White, in *Inorganic Nanopesticides and Nanofertilizers: A View from the Mechanisms of Action to Field Applications*, DOI: 10.1007/978-3-030-94155-0_9 (Eds: L. Fernandes Fraceto, H. W. Pereira de Carvalho, R. de Lima, S. Ghoshal, C. Santaella), Springer International Publishing, Cham **2022**, p. 271.
[59] Z. Yin, L. Song, H. Song, K. Hui, Z. Lin, Q. Wang, L. Xuan, Z. Wang, W. Gao, *Science of The Total Environment* **2020**, 741, 139962.
[60] J. Monod, *Annu. Rev. Microbiol.* **1949**, 3, 371.
[61] T. Chatterjee, B. K. Chatterjee, D. Majumdar, P. Chakrabarti, *Biochim. Biophys. Acta* **2015**, 1850, 299.
[62] M. Planchon, R. Ferrari, F. Guyot, A. Gélabert, N. Menguy, C. Chanéac, A. Thill, M. F. Benedetti, O. Spalla, *Colloids Surf. B Biointerfaces* **2013**, 102, 158.
[63] Q. Zhang, T. Xia, C. Zhang, *Environ. Sci. Technol.* **2020**, 54, 13186.
[64] S. Piçarra, E. Lopes, P. L. Almeida, H. de Lencastre, M. Aires-de-Sousa, *PLoS One* **2019**, 14, e0213151.
[65] C. Zollfrank, K. Gutbrod, P. Wechsler, J. P. Guggenbichler, *Materials Science and Engineering: C* **2012**, 32, 47.
[66] M. J. Hajipour, K. M. Fromm, A. Akbar Ashkarran, D. Jimenez de Aberasturi, I. R. d. Larramendi, T. Rojo, V. Serpooshan, W. J. Parak, M. Mahmoudi, *Trends in Biotechnology* **2012**, 30, 499.
[67] C. Cuny, M. Lesbats, S. Dukan, *Appl. Environ. Microbiol.* **2007**, 73, 885.
[68] M. D. Bradley, M. B. Beach, A. P. J. de Koning, T. S. Pratt, R. Osuna, *Microbiology* **2007**, 153, 2922.
[69] P. P. Fu, Q. Xia, H.-M. Hwang, P. C. Ray, H. Yu, *Journal of Food and Drug Analysis* **2014**, 22, 64.
[70] C. A. Juan, J. M. Pérez de la Lastra, F. J. Plou, E. Pérez-Lebeña, *International Journal of Molecular Sciences* **2021**, 22, 4642.
[71] A. Bhattacharyya, R. Chattopadhyay, S. Mitra, S. E. Crowe, *Physiological Reviews* **2014**, 94, 329.
[72] G. Pizzino, N. Irrera, M. Cucinotta, G. Pallio, F. Mannino, V. Arcoraci, F. Squadrito, D. Altavilla, A. Bitto, *Oxidative Medicine and Cellular Longevity* **2017**, 2017, 8416763.
[73] M. S. Chapekar, *Journal of Biomedical Materials Research* **2000**, 53, 617.
[74] H.-C. Flemming, J. Wingender, U. Szewzyk, *Biofilm Highlights*, **2011**.
[75] R. Mann, A. Holmes, O. McNeilly, R. Cavaliere, G. A. Sotiriou, S. A. Rice, C. Gunawan, *J. Nanobiotechnology* **2021**, 19, 291.
[76] J. Qu, D. Teng, X. Zhang, Q. Yang, P. Li, Y. Cao, *Ceramics International* **2022**, 48, 14451.
[77] M. A. Quinteros, V. Cano Aristizábal, P. R. Dalmasso, M. G. Paraje, P. L. Páez, *Toxicology in Vitro* **2016**, 36, 216.

[78] A. Staroń, O. Długosz, *Journal of Environmental Science and Health, Part A* **2021**, 56, 680.
[79] L. Kadirvelu, S. S. Sivaramalingam, D. Jothivel, D. D. Chithiraiselvan, D. Karaiyagowder Govindarajan, K. Kandaswamy, *Curr Res Microb Sci* **2024**, 6, 100231.
[80] M. Birkett, L. Dover, C. Cherian Lukose, A. Wasy Zia, M. M. Tambuwala, Á. Serrano-Aroca, *Int J Mol Sci* **2022**, 23.
[81] R. Gulati, S. Sharma, R. K. Sharma, *Polym Bull (Berl)* **2022**, 79, 5747.
[82] M. M. Querido, L. Aguiar, P. Neves, C. C. Pereira, J. P. Teixeira, *Colloids Surf B Biointerfaces* **2019**, 178, 8.
[83] A. Wojciechowska, M. Jakubczak, D. Moszczyńska, A. Wójcik, K. Prenger, M. Naguib, A. M. Jastrzębska, *Biomaterials Advances* **2023**, 153, 213581.
[84] A. M. Jastrzębska, E. Karwowska, A. R. Olszyna, A. Kunicki, *Surface and Coatings Technology* **2015**, 271, 225.